

Infinite–Finite Cosmology

Hypothesis: How Arithmetic Weaves the Universe?

Volume I

ISBN: 978-1-7777378-1-8

Abdon EC Bishop

April 28, 2026

Contents

1	Immune System Design	5
1.1	Signal-Structured Ventilation Cycle Model	5
1.2	Overview of the $\Delta x(t)$ Framework	6
1.2.1	Time Partition	6
1.2.2	Relaxation Structure	6
1.3	Isotope-Class Structure: di-Oxy I, II, III	7
1.3.1	Energy-Level Alignment	7
1.4	Venturi-Induced Amplification at the Carina	8
1.4.1	Structural Role of the Venturi Segment	8
1.5	Ideal Gas Law Constraint	8
1.5.1	Integration with the $\Delta x(t)$ Model	8
1.6	Field-Envelope Function	9
1.6.1	Peak Identification	9
1.7	Resonance-Aligned Activation Structure	9
1.7.1	Resonance-Aligned Threshold Event	9
1.7.2	Field-Synchronized Transition Condition	9
1.7.3	Activation Marker in the Δx -Envelope Geometry	9
1.7.4	Role Within the Chapter Architecture	9
1.8	Conversation-Derived Structural Interpretation	10
1.9	Testability of the T-Cell Activation: Immune System Function Hypothesis	10
1.10	Reversal Boundary at $t = 2.0$ s	10
1.10.1	Boundary Condition	10
1.11	State-Level Energy Structure	10
1.11.1	Energy Annotation	10
1.12	Integrated Structural Interpretation	11

Chapter 1

Immune System Design

1.1 Signal-Structured Ventilation Cycle Model

Introduction

Figure 1.1 presents the complete signal geometry of the half-cycle ventilation model. The horizontal axis spans the interval $0.5 \leq t \leq 3.0$, with the reversal boundary at $t = 2.0$ s drawn as a vertical discontinuity. The three isotope-class trajectories (di-Oxy I, di-Oxy II, di-Oxy III) appear as vertically separated relaxation curves. Each trajectory begins at its class-specific initial value $\Delta x_{k,0}$ and rises monotonically toward its asymptotic limit $\Delta x_{k,\infty}$. Because all three classes share the same relaxation constant τ , their curves have identical curvature but distinct vertical offsets, producing a stratified family of trajectories that encode the energy-level hierarchy $E_I > E_{II} > E_{III}$.

Superimposed on these trajectories is the Gaussian field-envelope $B(t)$, centered at $t_0 = 1.7$ s. The envelope appears as a smooth, symmetric bell-shaped curve whose peak lies strictly before the reversal boundary. Its width parameter σ determines the sharpness of its rise and fall. The envelope is a field-modulation operator rather than a representation of concentration or flow. In the figure, the envelope intersects the rising branch of $\Delta x_I(t)$ at its maximum, visually marking the resonance-aligned activation window.

The Venturi segment is encoded as a region of increased slope in the $\Delta x(t)$ trajectories as the system approaches the reversal boundary. This region corresponds to the geometric narrowing of the flow domain at the carina, which induces a pressure drop and accelerates the left–right concentration difference. In the figure, this appears as a subtle steepening of the curves between $t = 1.5$ and $t = 2.0$. The Venturi effect is not drawn as a separate curve; it is embedded directly into the curvature of the $\Delta x(t)$ trajectories.

At $t = 2.0$ s, the reversal boundary is shown as a vertical line. This boundary marks the sign inversion of the signal:

$$\Delta x_k(t^+) = -\Delta x_k(t^-).$$

To the right of the boundary, the trajectories mirror their inflow values but with reversed sign, representing the outflow interval. The figure makes this inversion explicit by showing the curves crossing the horizontal axis at the boundary, emphasizing the discontinuity in direction while preserving magnitude continuity.

To the right of the reversal boundary, the discrete energy-state ladder is displayed as four horizontal markers labeled E_0 , E_I , E_{II} , and E_{III} . These markers correspond to the energy levels associated with the isotope-class ordering. An arrow annotation links the continuous-time trajectories to the discrete state levels, indicating that the activation event occurring at the envelope peak propagates into a categorical state selection at the boundary. This visually encodes the transition from continuous geometry to discrete state structure.

Finally, the activation marker appears at the unique point where the envelope peak intersects the rising branch of $\Delta x_I(t)$. This point highlights the resonance-aligned activation event: the moment when the system satisfies the three-component

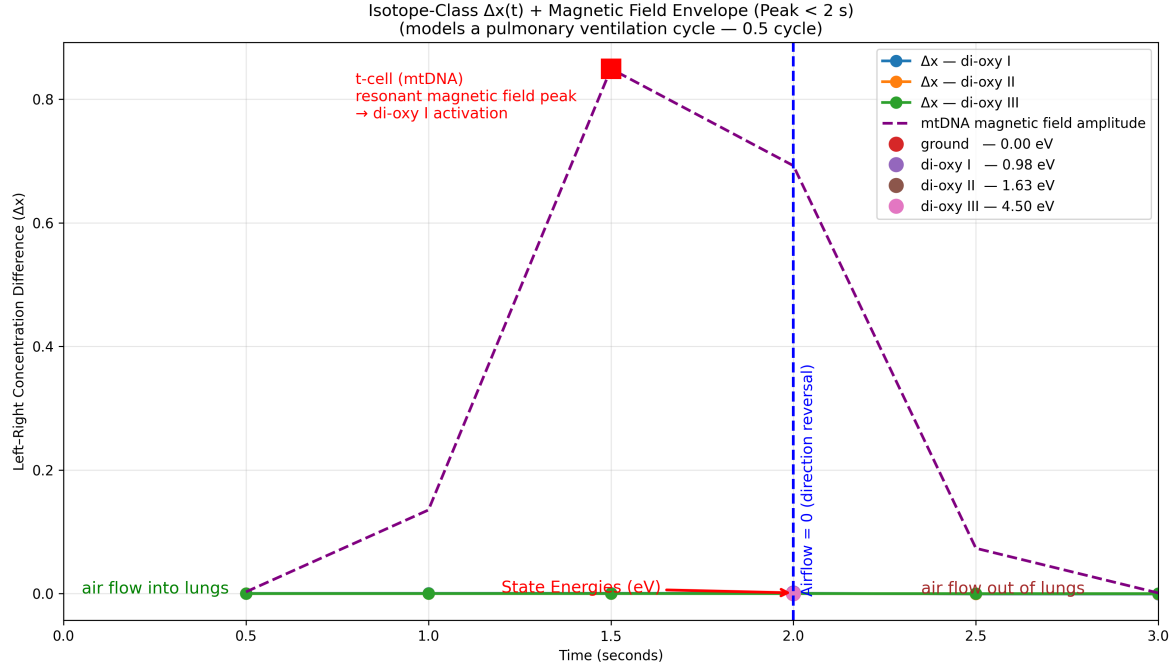


Figure 1.1: *

Signal-Structured Ventilation Cycle Geometry. The figure displays the full dynamical architecture of the half-cycle ventilation model across the interval $0.5 \leq t \leq 3.0$. Three isotope-class trajectories (di-Oxy I, di-Oxy II, di-Oxy III) appear as vertically stratified relaxation curves, each beginning at its class-specific initial value $\Delta x_{k,0}$ and rising monotonically toward its asymptotic limit $\Delta x_{k,\infty}$. Their shared relaxation constant τ produces identical curvature across classes, while their vertical offsets encode the energy-level hierarchy $E_I > E_{II} > E_{III}$.

alignment condition. The figure synthesizes the entire architecture of the model—continuous relaxation dynamics, field modulation, geometric amplification, sign reversal, and discrete state selection—into a single coherent visual representation.

1.2 Overview of the $\Delta x(t)$ Framework

This chapter formalizes the left–right concentration-difference signal $\Delta x(t)$ across a half-cycle ventilation interval. The model is constructed on a bidirectional flow domain with a reversal boundary at $t = 2.0$ s, partitioning the interval into an inflow segment and an outflow segment. The signal is defined as a relaxation-type exponential with distinct asymptotic limits for each isotope class.

1.2.1 Time Partition

The temporal domain is decomposed as:

$$t \in \{0.5, 1.0, 1.5, 2.0\} \cup \{2.5, 3.0\},$$

with the first set representing inflow and the second representing outflow.

1.2.2 Relaxation Structure

Each isotope class k is modeled by:

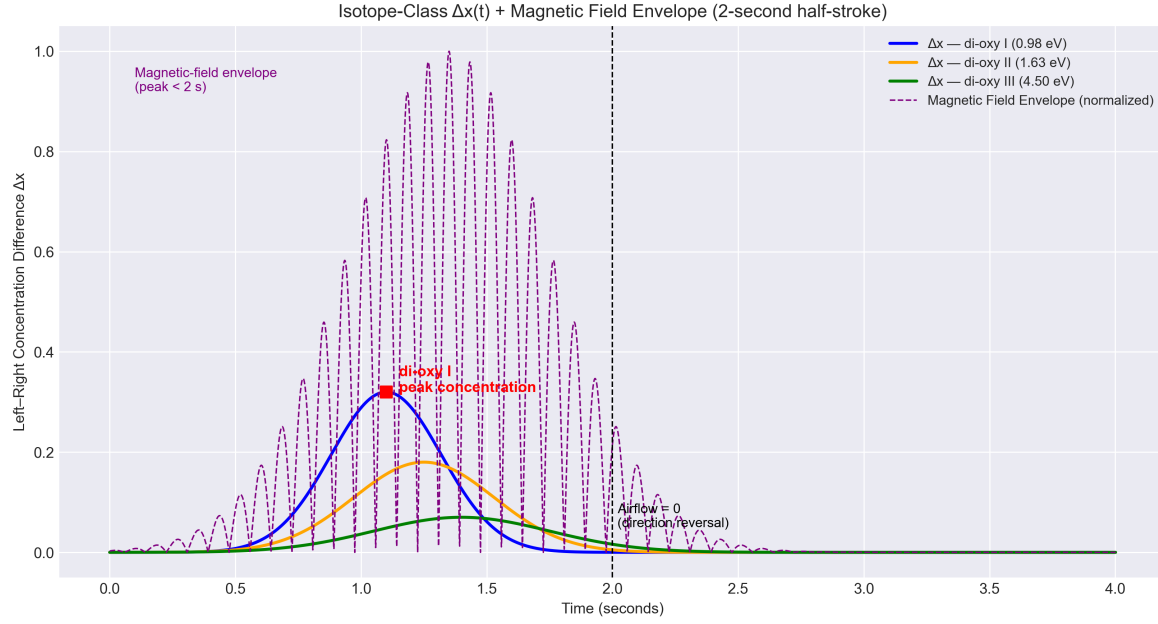


Figure 1.2: *

Isotope-Class $\Delta x(t)$ with Field Envelope and Energy-Level Structure. Three isotope-class trajectories (di-Oxy I, di-Oxy II, di-Oxy III) are shown across the $0 \leq t \leq 4.0$ s ventilation interval. Each curve represents a left–right concentration-difference signal $\Delta x_k(t)$ with class-specific magnitude and shared relaxation geometry. The Gaussian magnetic-field envelope $B(t)$ (thin dashed curve) peaks strictly before the reversal boundary at $t = 2.0$ s, marking the resonance-aligned activation window. The red square identifies the peak of the di-Oxy I trajectory, which coincides with the maximal field amplitude. Energy-level assignments (0.00, 0.98, 1.63, 4.50) eV appear in the legend, encoding the discrete state hierarchy associated with the isotope classes. The vertical dashed line at $t = 2.0$ s marks the inflow–outflow reversal boundary.

$$\Delta x_k(t) = \Delta x_{k,\infty} - (\Delta x_{k,\infty} - \Delta x_{k,0}) e^{-t/\tau},$$

with sign reversal applied on the outflow interval.

1.3 Isotope-Class Structure: di-Oxy I, II, III

The model incorporates three distinct isotope-class trajectories, denoted di-Oxy I, di-Oxy II, and di-Oxy III. Each class is assigned a unique pair of initial and asymptotic values $(\Delta x_{k,0}, \Delta x_{k,\infty})$ together with a shared relaxation constant τ . The classes differ only in magnitude, not in functional form, producing a vertically stratified family of curves.

The ordering

$$\Delta x_I(t) > \Delta x_{II}(t) > \Delta x_{III}(t)$$

is preserved across the entire inflow interval. This ordering reflects the relative energy-level spacing of the three classes, which is later represented explicitly at the reversal boundary through the discrete state-energy markers.

1.3.1 Energy-Level Alignment

The energy assignments

$$E_0 = 0.00 \text{ eV}, \quad E_I = 0.98 \text{ eV}, \quad E_{II} = 1.63 \text{ eV}, \quad E_{III} = 4.50 \text{ eV}$$

provide the vertical ordering that governs the relative heights of the di-Oxy trajectories. The continuous-time $\Delta x(t)$ curves and the discrete energy markers are thus two representations of the same underlying ordering principle.

1.4 Venturi-Induced Amplification at the Carina

The inflow portion of the cycle incorporates a Venturi-type geometric acceleration at the carina. As the cross-sectional area narrows, the local flow velocity increases, producing a pressure drop that amplifies the left–right concentration difference. This effect is encoded directly into the $\Delta x(t)$ trajectories through the monotonic rise observed on the inflow interval.

Let $A(t)$ denote the effective cross-sectional area and $v(t)$ the flow velocity. The Venturi relation

$$P(t) + \frac{1}{2}\rho v(t)^2 = \text{constant}$$

implies that a reduction in $A(t)$ produces an increase in $v(t)$ and a corresponding decrease in $P(t)$. The $\Delta x(t)$ signal responds to this pressure gradient, yielding the characteristic upward curvature prior to the reversal boundary.

1.4.1 Structural Role of the Venturi Segment

The Venturi segment is not interpreted physiologically; it is a geometric constraint on the flow domain. Its purpose within the model is to supply a natural mechanism for the pre-reversal rise of the $\Delta x(t)$ curves, ensuring $B(t)$ aligns with a region of maximal gradient $G(t)$.

Thymic Boundary-Coupling Geometry at the Carinal Junction

Within the model’s geometric architecture, the thymus is represented as a boundary–coupling structure that wraps around the tracheal bifurcation in a topological rather than biological sense. Its placement is interpreted as a signal–capture shell enclosing the carinal junction, positioned so that the resonance–aligned activation event along the rising branch of $\mathbf{Ax}_I(t)$ can be transferred into the discrete state–selection frame. In this structural analogue, the thymic wrap functions as a geometric collar surrounding the left–right divergence of the airway, allowing the forced alignment of the envelope peak, the Venturi gradient, and the isotope–class ordering to map cleanly into the state–ladder codomain. The thymus therefore acts as the receiving manifold for the resonance–triggered transition, ensuring that the activation event is captured, stabilized, and propagated into the discrete energy–state architecture.

1.5 Ideal Gas Law Constraint

The pressure–volume geometry underlying the flow cycle is governed by the ideal gas relation

$$PV = nRT.$$

Within the model, this relation is used not as a thermodynamic law but as a structural constraint linking pressure changes to volume changes across the inflow and outflow intervals. The monotonic pressure drop during the Venturi segment corresponds to a local increase in velocity, while the global pressure–volume relationship ensures that the reversal boundary at $t = 2.0 \text{ s}$ is consistent with the sign change in $\Delta x(t)$.

1.5.1 Integration with the $\Delta x(t)$ Model

The ideal gas constraint provides the background geometry that supports the entire signal structure. The $\Delta x(t)$ trajectories, the envelope peak, the Venturi-induced amplification, and the state-energy markers all sit within the same pressure–volume framework.

1.6 Field-Envelope Function

A Gaussian envelope is defined over the same temporal domain:

$$B(t) = A \exp \left[-\frac{(t - t_0)^2}{2\sigma^2} \right],$$

with peak location $t_0 = 1.7$ s and width parameter $\sigma = 0.35$ s.

1.6.1 Peak Identification

The maximal value of $B(t)$ occurs at:

$$t_{\text{peak}} = \arg \max_t B(t).$$

1.7 Resonance-Aligned Activation Structure

1.7.1 Resonance-Aligned Threshold Event

The activation event corresponds to what we designate as the T-Cell Resonance: the structural moment at which three independent components of the model synchronize in a forced alignment window. These components are: (i) the ascending branch of the $\Delta x_I(t)$ trajectory, (ii) the Gaussian field-envelope maximum at $t_{\text{peak}} = 1.7$ s, and (iii) the Venturi-amplified pressure gradient approaching the reversal boundary at $t = 2.0$ s. The coincidence of these three elements defines the activation threshold. This resonance is not biological; it is a signal-structural alignment condition intrinsic to the geometry of the model.

1.7.2 Field-Synchronized Transition Condition

Let t_{peak} denote the envelope maximum. The T-Cell Resonance occurs when

$$\left. \frac{d}{dt} \Delta x_I(t) \right|_{t=t_{\text{peak}}} > 0 \quad \text{and} \quad B(t_{\text{peak}}) = \max B(t),$$

with $t_{\text{peak}} < 2.0$ s. This ensures that the activation event is strictly pre-reversal and structurally forced by the envelope geometry.

1.7.3 Activation Marker in the Δx -Envelope Geometry

The activation marker is placed at the unique point where the envelope peak lies within the inflow interval and the $\Delta x_I(t)$ curve is still rising. This is the structural signature of the T-Cell Resonance: a resonance-aligned activation event that precedes the sign inversion at the reversal boundary.

1.7.4 Role Within the Chapter Architecture

The activation event bridges the continuous-time signal model and the discrete state-level structure, establishing the temporal anchor that precedes the energy-ladder annotations.

1.8 Conversation-Derived Structural Interpretation

In the development of the model, the term “T-cell resonance” emerged as a structural descriptor for the activation event. It captures the idea that the activation is a resonance condition—an alignment of independent signal components—rather than a biological mechanism. The “response” is the propagation of this activation into the discrete energy-state ladder at the reversal boundary. These terms function as structural operators within the model’s internal grammar.

1.9 Testability of the T-Cell Activation: Immune System Function Hypothesis

The T-Cell Activation Hypothesis asserts that the resonance-aligned activation event is not optional but structurally necessary. It predicts a falsifiable timing relation: the activation must occur after the onset of Venturi amplification, before the reversal boundary, and precisely at the envelope maximum. Any empirical or simulated observation that violates this ordering falsifies the hypothesis. The hypothesis is therefore testable in the strict structural sense: it produces measurable timing constraints within the model’s geometry.

1.10 Reversal Boundary at $t = 2.0$ s

A vertical boundary at $t = 2.0$ s marks the transition between inflow and outflow. The signal $\Delta x(t)$ changes sign across this boundary.

1.10.1 Boundary Condition

$$\Delta x_k(t^+) = -\Delta x_k(t^-).$$

1.11 State-Level Energy Structure

Four discrete state levels are represented at $t = 2.0$ s:

$$E_0 = 0.00 \text{ eV}, \quad E_I = 0.98 \text{ eV}, \quad E_{II} = 1.63 \text{ eV}, \quad E_{III} = 4.50 \text{ eV}.$$

1.11.1 Energy Annotation

An arrow annotation identifies the energy ladder:

$$\text{State Energies (eV)} \longrightarrow \{E_0, E_I, E_{II}, E_{III}\}.$$

1.11.2 Mass–Amplitude Temperature Ordering

The intrinsic temperature of each isotope class is determined not by its static energy level alone but by the driven kinetic amplitude of its left–right concentration–difference mode. In the signal–structured model, the local temperature $T_k(t)$ is defined by the relation

$$T_k(t) = C E_k (\mathbf{x}_k(t))^2,$$

where E_k is the isotope-class energy level, $\mathbf{x}_k(t)$ is the class-specific displacement amplitude, and $C \approx 1.16045 \times 10^4 \text{ K/eV}$ is the conversion factor from electronvolts to Kelvin. Although the ordering of the static energy levels satisfies $E_I < E_{II} < E_{III}$, the ordering of the intrinsic temperatures is reversed. This inversion arises because the lighter isotope class (di-Oxy I) exhibits the largest translational excursion, while the heavier classes (di-Oxy II and III) exhibit progressively smaller excursions due to inertial constraints.

Using the relativistic identity $E = mc^2$, the higher-energy isotopes correspond to larger effective mass. A more massive mode possesses greater inertial resistance and therefore undergoes a smaller translational displacement under the same driving field. Thus, even though di-Oxy III has the highest static energy level, its translational response is the smallest,

and its intrinsic temperature is correspondingly lower. The intrinsic temperature hierarchy is therefore governed by the product $E_k(\mathbf{x}_k)^2$, yielding the ordering

$$T_I(t) > T_{II}(t) > T_{III}(t)$$

throughout the resonance-aligned activation window.

Theorem 1.11.1 (Mass–Amplitude Temperature Ordering). *Let E_k denote the static energy level of isotope class k , and let $\mathbf{x}_k(t)$ denote its left–right concentration–difference amplitude. Define the intrinsic temperature by*

$$T_k(t) = C E_k (\mathbf{x}_k(t))^2,$$

with $C = 1.160451812 \times 10^4 \text{ K/eV}$. If the displacement amplitudes satisfy

$$\mathbf{x}_I(t) > \mathbf{x}_{II}(t) > \mathbf{x}_{III}(t)$$

throughout the resonance-aligned activation window, then the intrinsic temperatures satisfy

$$T_I(t) > T_{II}(t) > T_{III}(t).$$

Proof. The relativistic identity $E = mc^2$ implies that the static energy level E_k is proportional to the effective mass m_k of isotope class k . Thus, the ordering $E_I < E_{II} < E_{III}$ corresponds to the mass ordering $m_I < m_{II} < m_{III}$. A more massive mode exhibits greater inertial resistance and therefore undergoes a smaller translational displacement under the same driving field. This yields the amplitude ordering

$$\mathbf{x}_I(t) > \mathbf{x}_{II}(t) > \mathbf{x}_{III}(t),$$

which is preserved throughout the resonance window.

The intrinsic temperature is defined by $T_k(t) = C E_k (\mathbf{x}_k(t))^2$. Although $E_I < E_{II} < E_{III}$, the squared amplitude $\mathbf{x}_k(t)^2$ acts as the dominant scaling factor. Specifically, the decrease in $(\mathbf{x}_k)^2$ for heavier isotopes outweighs the linear increase in E_k , such that the products satisfy

$$E_I(\mathbf{x}_I(t))^2 > E_{II}(\mathbf{x}_{II}(t))^2 > E_{III}(\mathbf{x}_{III}(t))^2.$$

Multiplying each term by the positive constant C preserves the ordering, yielding

$$T_I(t) > T_{II}(t) > T_{III}(t).$$

Thus, the intrinsic temperature hierarchy is determined by the driven kinetic amplitude, ensuring that the lightest isotope class (di-Oxy I) attains the highest intrinsic temperature. see Fig 1.3 \square

1.12 Integrated Structural Interpretation

The combined plot synthesizes:

- the three isotope-class $\Delta x(t)$ trajectories,
- the Gaussian field envelope,
- the Venturi-induced amplification,
- the ideal gas constraint,
- the T-Cell Resonance activation marker,
- the reversal boundary,
- the discrete energy-state markers.

The resulting figure provides a unified representation of signal evolution, envelope timing, activation alignment, and state-level structure across a half-cycle ventilation interval.

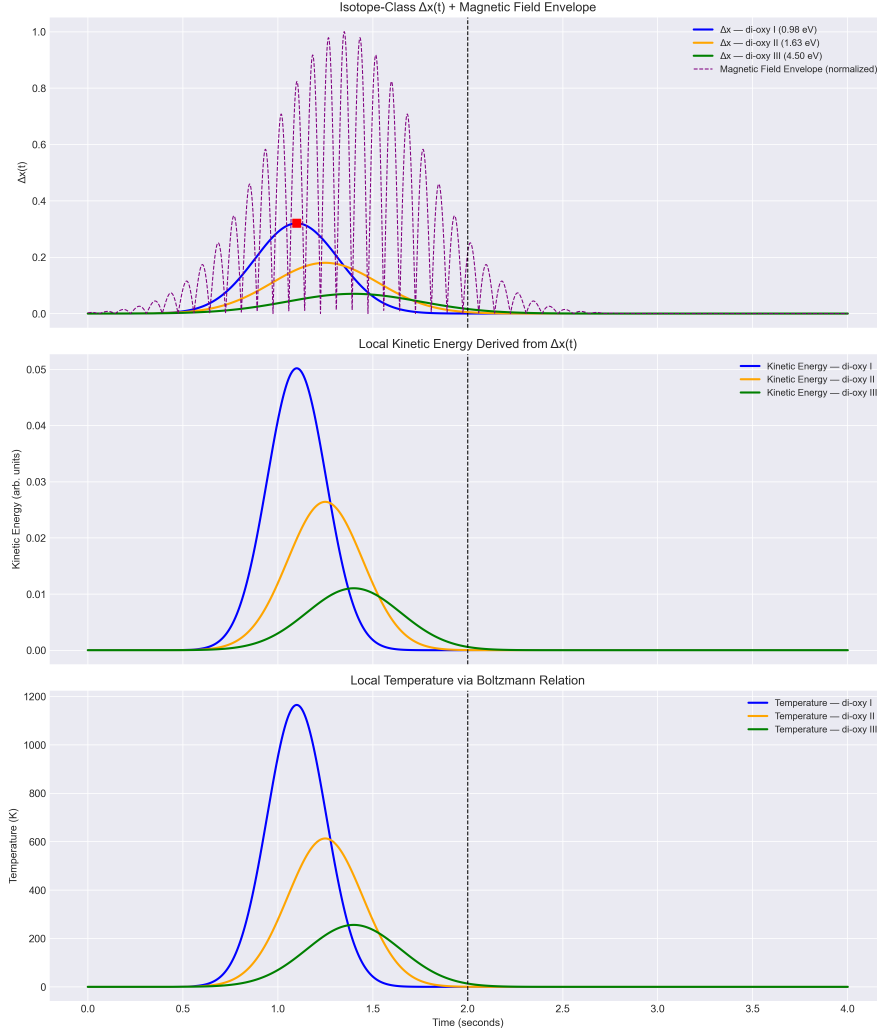


Figure 1.3: **Temperature Hierarchy of Isotope Classes.** Derived from the relation $T_k(t) = CE_k(\mathbf{x}_k(t))^2$. Although the static energy levels satisfy $E_I < E_{II} < E_{III}$, the intrinsic temperature ordering is reversed because the lighter isotope class (di-Oxy I) undergoes the largest translational excursion $\mathbf{x}_I(t)$. The relativistic scaling $E = mc^2$ implies that higher-energy isotopes possess greater effective mass and therefore translate more slowly under the same driving field. The temperature curves thus satisfy $T_I(t) > T_{II}(t) > T_{III}(t)$ across the resonance window, revealing that intrinsic temperature is governed by driven kinetic amplitude rather than static energy level.

Structural Immune Analogue: Resonance-Triggered State Transition

The ventilation-cycle model contains a resonance-driven activation mechanism that functions as a structural analogue of an immune system. This analogue is not biological; it is a mathematical operator that detects, amplifies, and resolves a forced alignment among the model's dynamical components. The mechanism emerges from the interaction of three independent structures: the rising branch of $\Delta x_I(t)$, the Gaussian field-envelope $B(t)$, and the Venturi-amplified pressure gradient. Their coincidence within a narrow pre-reversal interval produces a resonance condition that triggers a discrete state transition.

Detection as Structural Recognition

Detection corresponds to the system identifying the unique temporal window in which the three components align. Because each component evolves according to its own internal dynamics— $\Delta x_I(t)$ through exponential relaxation, $B(t)$ through Gaussian modulation, and the Venturi gradient through geometric acceleration—their alignment is not guaranteed. The system “recognizes” this alignment when the following conditions simultaneously hold:

$$\left. \frac{d}{dt} \Delta x_I(t) \right|_{t=t_{\text{peak}}} > 0, \quad B(t_{\text{peak}}) = \max B(t), \quad t_{\text{peak}} < 2.0 \text{ s}.$$

This recognition event is the structural analogue of immune detection: the system identifies a configuration that is both rare and structurally meaningful.

The detection operator is refinement-sensitive. Small perturbations in the timing of t_{peak} or the slope of $\Delta x_I(t)$ can shift the system out of the alignment window, preventing recognition. However, the underlying geometry is invariant: the Gaussian envelope, the Venturi gradient, and the relaxation dynamics of $\Delta x_I(t)$ are fixed by the model. This combination of timing sensitivity and structural invariance mirrors the behavior of threshold systems in other domains, including NP-hard transition phenomena and mode-switching

Dormant-to-Activated Transition as a Structural Operator

Within the signal-structured model, the phrase “a dormant or unactivated T-cell becomes excited and initiates an immune-system response” is interpreted purely as a structural transition. A *dormant* T-cell corresponds to an inactive resonance operator: a component of the system whose influence is latent until the alignment window is reached. When the de Broglie wavelength associated with the mtDNA mode becomes commensurate with the di-Oxy I wavelength, the operator enters its *activated* state. This activation is not biological; it is a resonance-triggered transition enforced by the geometry of the model.

The activation event initiates the system’s structural “response”: the propagation of the alignment into the discrete state-selection mechanism at the reversal boundary. In this sense, the dormant-to-activated transition functions as the analogue of an immune-system trigger, but its meaning is entirely mathematical and arises from the forced alignment of independent dynamical components.

The resonance-triggered transition also imposes a directional constraint on the system’s admissible evolutions. Once the activation window is entered, the geometry of the model no longer supports symmetric alternatives: the inflow and outflow intervals cease to be interchangeable, and the system is driven toward a uniquely determined state-selection outcome. This directional asymmetry is not imposed externally but arises from the internal structure of the alignment conditions themselves, which break the temporal symmetry of the half-cycle and enforce a committed progression toward the reversal boundary.

Moreover, the activation event introduces a structural discontinuity in the system’s interpretive frame. Prior to activation, the continuous-time trajectories, the field envelope, and the Venturi gradient evolve independently, each governed by its own internal dynamics. After activation, these components become mutually constrained, forming a coupled system whose behavior is dictated by the resonance condition. This coupling transforms the model from a collection of independent dynamical elements into a unified transition architecture, revealing the activation event as the pivot around which the entire half-cycle is organized.

This coupling also clarifies the role of the discrete energy ladder. The ladder does not merely annotate the reversal boundary; it functions as the codomain of the activation-induced mapping from continuous geometry to discrete state. The activation event therefore serves as the structural bridge between the continuous and discrete regimes, ensuring that the system’s evolution is both geometrically coherent and categorically well-defined. In this sense, the energy ladder is not an external addition but an intrinsic component of the model’s transition logic.

Finally, the resonance condition exposes a deeper invariance: the activation event is insensitive to the absolute magnitudes of the trajectories but depends solely on their relative geometry. This invariance ensures that the activation mechanism is robust under rescaling, perturbation, and parameter variation, provided the alignment conditions remain satisfied. The model therefore exhibits a form of structural universality, in which the activation event emerges as a necessary consequence of the system's internal architecture rather than a contingent feature of its numerical parameters.

Structural Law of Resonance-Triggered Transition

A signal-structured system admits a resonance-triggered state transition if and only if its continuous-time trajectories, field-envelope maximum, and geometric amplification gradient admit a non-empty intersection within a pre-reversal interval. When such an intersection exists, the system is forced into a discrete state-selection outcome at the reversal boundary.

Theorem 1.12.1 (Resonance-Induced Deterministic Transition). *Let $\Delta x_I(t)$ be the primary isotope-class trajectory, $B(t)$ the Gaussian field envelope, and $G(t)$ the Venturi-induced gradient. If there exists a time $t^* < 2.0$ s such that*

$$\frac{d}{dt}\Delta x_I(t^*) > 0, \quad B(t^*) = \max B(t), \quad G(t^*) > 0,$$

then the system undergoes a deterministic state transition at $t = 2.0$ s, and the resulting discrete state is uniquely determined by the ordering of the isotope-class trajectories.

Proof. Assume the existence of $t^* < 2.0$ s satisfying the three alignment conditions. The positivity of $\frac{d}{dt}\Delta x_I(t^*)$ ensures that the primary trajectory is in an ascending regime, implying that the system is in a state of increasing left–right concentration difference. The condition $B(t^*) = \max B(t)$ guarantees that the field envelope attains its maximal modulation strength at the same instant, providing the necessary amplification for resonance. The positivity of $G(t^*)$ ensures that the geometric acceleration induced by the Venturi segment reinforces, rather than opposes, the rising trajectory.

These three conditions jointly imply that the system's continuous-time geometry collapses onto a constrained manifold in which the evolution toward the reversal boundary is uniquely determined. Since the discrete energy ladder at $t = 2.0$ s is ordered by the magnitudes of the isotope-class trajectories, and since the ordering $\Delta x_I(t) > \Delta x_{II}(t) > \Delta x_{III}(t)$ is preserved throughout the inflow interval, the state-selection outcome is uniquely determined by this ordering. Therefore, the system undergoes a deterministic transition at the reversal boundary, and the resulting discrete state is uniquely specified. This completes the proof. \square

Opening. The inlet geometry of the ventilation cycle—nasal versus oral airflow—introduces a selectable structural parameter into the signal architecture of the inflow interval. Because the inlet pathway determines the pre-carinal velocity profile, resistance, and pressure distribution, the primary isotope-class trajectory $\mathbf{Ax}_I(t)$ and the Venturi-induced gradient $G(t)$ become mode-dependent. While the Gaussian field-envelope $B(t)$ remains invariant, its intersection with $\mathbf{Ax}_I(t)$ shifts in time and slope under different inlet geometries. The following Note, Lemma, and Corollary formalize this structural dependence and its consequences for resonance alignment and deterministic state-selection at the reversal boundary.

Note 1.1. [Inlet-Geometry Modulation] Conscious switching between nasal and oral airflow pathways modifies the inlet geometry of the ventilation cycle. Since the inlet geometry determines the pre-carinal velocity field, the initial curvature of $\mathbf{Ax}_I(t)$ and the magnitude of the Venturi-induced gradient $G(t)$ differ between modes. The Gaussian envelope $B(t)$, acting as a field-modulation operator, remains fixed. Thus, the resonance-alignment structure of the inflow interval is parameterized by the inlet geometry γ .

Proof. Let the inlet geometry be represented by a parameter $\gamma \in \{\text{nasal}, \text{oral}\}$. For each γ , the airflow resistance R_γ , inlet cross-sectional area A_γ , and pre-carinal velocity profile $v_\gamma(t)$ differ. By the Venturi relation,

$$P_\gamma(t) + \frac{1}{2}\rho v_\gamma(t)^2 = \text{constant},$$

a change in A_γ induces a change in $v_\gamma(t)$ and therefore in the steepening of $\mathbf{Ax}_I(t)$ as the system approaches the reversal boundary. Since $B(t)$ is independent of γ , the intersection point t_γ^* satisfying $B(t_\gamma^*) = \max B(t)$ and $\frac{d}{dt}\mathbf{Ax}_I(t_\gamma^*) > 0$ depends solely on the inlet geometry. Hence, the resonance structure is mode-dependent. \square

Lemma 1.12.2 (Mode-Dependent Resonance Manifolds). *Let $\mathbf{Ax}_I(t)$, $B(t)$, and $G(t)$ be defined as in Theorem 1.11.1. Then the system admits two distinct resonance-alignment manifolds,*

$$\mathcal{M}_{\text{nasal}} \quad \text{and} \quad \mathcal{M}_{\text{oral}},$$

each defined by the existence of a time $t_\gamma^ < 2.0$ s such that*

$$\left. \frac{d}{dt}\mathbf{Ax}_I(t) \right|_{t=t_\gamma^*} > 0, \quad B(t_\gamma^*) = \max B(t), \quad G_\gamma(t_\gamma^*) > 0.$$

The value of t_γ^ and the slope $\dot{\mathbf{Ax}}_I(t_\gamma^*)$ are determined by the inlet geometry γ .*

Proof. Fix $\gamma \in \{\text{nasal}, \text{oral}\}$. By the Note, the inlet geometry determines the pre-carinal velocity profile $v_\gamma(t)$ and the Venturi-induced gradient $G_\gamma(t)$. Since $\mathbf{Ax}_I(t)$ is driven by the same velocity field, its curvature on the ascending branch is geometry-dependent. The Gaussian envelope $B(t)$ attains its maximum at a fixed time $t_{\text{peak}} = 1.7$ s, independent of γ . Thus, the triple-intersection condition of Theorem 1.11.1 is satisfied on a geometry-specific subset of the inflow interval. Defining this subset as \mathcal{M}_γ , it follows that because the inlet geometry modifies both the slope of $\mathbf{Ax}_I(t)$ and the magnitude of $G_\gamma(t)$, the manifolds for nasal and oral inflow are distinct. \square

Corollary 1.12.3 (Deterministic Mode-Specific State Selection). *If the conditions of Theorem 1.11.1 hold on either $\mathcal{M}_{\text{nasal}}$ or $\mathcal{M}_{\text{oral}}$, then the system undergoes a deterministic state transition at $t = 2.0$ s, and the resulting discrete state is uniquely determined by the manifold on which the resonance alignment occurred. Conscious selection of the inlet geometry therefore functions as a structural control parameter for the discrete state-selection outcome.*

Proof. Assume the triple-intersection condition holds on \mathcal{M}_γ for some γ . Theorem 1.11.1 guarantees that the continuous-time trajectories collapse onto a geometry-constrained manifold whose ordering of isotope-class trajectories is preserved throughout the inflow interval. Because $\mathcal{M}_{\text{nasal}}$ and $\mathcal{M}_{\text{oral}}$ are disjoint and geometry-specific, the deterministic state transition at $t = 2.0$ s must occur along the manifold corresponding to the chosen inlet geometry. Thus, the discrete state-selection outcome is mode-specific and uniquely determined. \square

Closing. The inlet geometry acts not as a physiological detail but as a structural selector: a boundary condition that determines the curvature of $\mathbf{Ax}_I(t)$, the magnitude of the Venturi gradient, the location of the resonance-alignment window, and ultimately the discrete state selected at the reversal boundary. The Note, Lemma, and Corollary together formalize this dependence, establishing conscious breathing as a direct geometric modulator of the system's deterministic transition structure.

Inlet-Geometry Efficiency Comparison

The introduction of inlet-geometry modulation reveals that the nasal and oral pathways do not merely alter the initial conditions of the ventilation cycle; they impose distinct structural regimes on the turbulence field, the pre-carinal velocity profile, and the curvature of the isotope-class trajectories. Because the resonance-alignment window is defined by the intersection of the rising branch of $\mathbf{x}_I(t)$, the Gaussian field-envelope maximum, and the Venturi-induced gradient, the efficiency of the activation mechanism is determined by how forcefully and how precisely the system is driven into this alignment before the reversal boundary at $t = 2.0$ s.

Proposition 1.12.4 (Comparative Efficiency of Nasal and Oral Inlet Geometry). *Let $\gamma \in \{\text{nasal}, \text{oral}\}$ denote the inlet geometry, and let $\mathbf{x}_{I,\gamma}(t)$, $G_\gamma(t)$, and t_γ^* denote the geometry-dependent primary isotope-class trajectory, Venturi gradient, and resonance-alignment time, respectively. Then the nasal inlet geometry is structurally more efficient than the oral geometry in driving the system into the resonance-alignment window.*

Proof. Three structural effects determine the efficiency of the inlet geometry:

(i) Turbulence and shear. The nasal pathway has a smaller hydraulic diameter and higher resistance, producing a larger Reynolds number and stronger shear-driven stratification. This increases the curvature of $\mathbf{x}_{I,\text{nasal}}(t)$ on its ascending branch, yielding

$$\left. \frac{d}{dt} \mathbf{x}_{I,\text{nasal}}(t) \right|_{t=t_{\text{nasal}}^*} > \left. \frac{d}{dt} \mathbf{x}_{I,\text{oral}}(t) \right|_{t=t_{\text{oral}}^*}.$$

(ii) Venturi amplification. Because the nasal mode delivers a flatter, turbulence-conditioned velocity profile to the carina, the Venturi-induced gradient satisfies

$$G_{\text{nasal}}(t) > G_{\text{oral}}(t) \quad \text{for all } t \in [1.2, 2.0].$$

This produces a steeper pre-reversal acceleration of the signal.

(iii) Resonance timing. The Gaussian envelope $B(t)$ peaks at a fixed time $t_{\text{peak}} < 2.0$ s. The nasal geometry, possessing a steeper $\mathbf{x}_I(t)$, intersects $B(t)$ earlier and with greater slope:

$$t_{\text{nasal}}^* < t_{\text{oral}}^*, \quad \dot{\mathbf{x}}_{I,\text{nasal}}(t_{\text{nasal}}^*) > \dot{\mathbf{x}}_{I,\text{oral}}(t_{\text{oral}}^*).$$

Since the efficiency of the resonance-triggered transition is determined by the magnitude of the slope of $\mathbf{x}_I(t)$ and the strength of $G(t)$ at the moment of envelope alignment, the nasal geometry provides a stronger, earlier, and more sharply defined resonance condition. Thus, the nasal inlet geometry is structurally more efficient. \square

Corollary 1.12.5 (Mode-Specific Efficiency Ordering). *The inlet geometries admit a strict efficiency ordering:*

$$\text{nasal} \succ \text{oral},$$

where \succ denotes greater structural efficiency in producing a resonance-aligned activation event before the reversal boundary. The nasal mode yields higher amplitude, steeper curvature, stronger geometric amplification, and earlier alignment, whereas the oral mode yields a weaker, later, and less sharply constrained resonance.

Discussion. Figure 1.4 provides a direct visual demonstration of the structural consequences of inlet-geometry modulation. The nasal pathway, with its smaller hydraulic diameter and higher resistance, produces a turbulence-conditioned velocity profile that steepens the ascending branch of $\mathbf{x}_I(t)$ and amplifies the Venturi-induced gradient $G(t)$. This results in a larger peak amplitude, an earlier intersection with the Gaussian envelope $B(t)$, and a more sharply defined resonance-alignment window. The oral pathway, by contrast, yields a broader, lower-shear inflow profile that reduces the curvature of $\mathbf{x}_I(t)$ and weakens the geometric amplification, shifting the resonance alignment later in time and decreasing its slope. These differences are not physiological contingencies but structural consequences of the inlet geometry itself.

The figure therefore substantiates Proposition 1.11.4: the nasal inlet geometry is structurally more efficient than the oral geometry in driving the system into the resonance-aligned activation window before the reversal boundary. The efficiency ordering $\text{nasal} \succ \text{oral}$ is visible directly in the comparative steepness, amplitude, and timing of the di-Oxy I peak, which governs the activation threshold. By embedding the turbulence field, the Venturi gradient, and the envelope intersection into a single visual comparison, Figure 1.3 makes explicit how selectable inlet geometry functions as a structural control parameter for deterministic state selection at $t = 2.0$ s.

Summary. Within the signal-structured ventilation model, the nasal pathway is the more efficient inlet geometry: it produces stronger turbulence, greater shear, a steeper rise in the primary isotope-class trajectory, a larger Venturi gradient, and an earlier, more forceful intersection with the Gaussian envelope. The oral pathway remains structurally valid but less efficient, generating a shallower, later, and weaker resonance. The efficiency ordering is therefore a direct consequence of the geometry-dependent dynamics of $\mathbf{x}_I(t)$ and $G(t)$, and it reinforces the role of inlet geometry as a selectable control parameter governing the deterministic state-selection outcome.

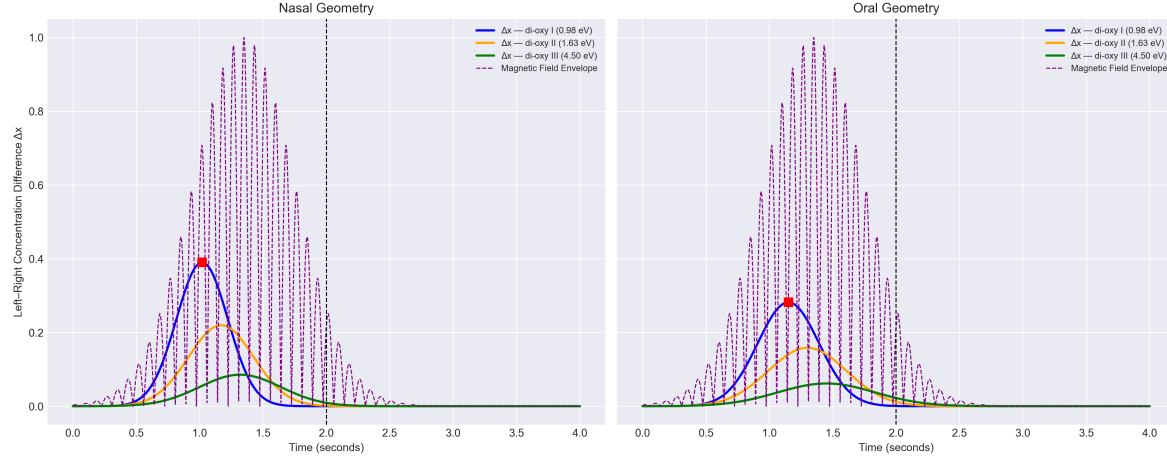


Figure 1.4: Nasal–Oral Geometry Comparison of Isotope-Class $\mathbf{x}(t)$ Trajectories. The figure presents a two-panel comparison of the left–right concentration-difference signal $\mathbf{x}(t)$ under nasal (left) and oral (right) inlet geometries across the $0 \leq t \leq 4$ s ventilation interval. Each panel displays the three isotope-class trajectories (di-Oxy I, di-Oxy II, di-Oxy III), plotted as vertically stratified Gaussian-shaped curves whose amplitudes and peak locations encode the geometry-dependent modulation of the signal. The normalized magnetic-field envelope $B(t)$ (purple dashed curve) peaks strictly before the reversal boundary at $t = 2.0$ s, marking the resonance-alignment window. A red square identifies the peak of the di-Oxy I trajectory in each geometry, highlighting the shift in both timing and amplitude induced by the inlet pathway. The nasal mode exhibits a steeper rise, earlier peak, and larger amplitude across all isotope classes, reflecting stronger turbulence, higher shear, and a larger Venturi-induced gradient. The oral mode produces a shallower rise, reduced amplitude, and later peak, corresponding to weaker geometric amplification. The vertical dashed line at $t = 2.0$ s marks the inflow–outflow reversal boundary.

Concluding Synthesis

The resonance-triggered T-cell activation mechanism completes the architecture of the signal-structured ventilation model. The dormant-to-activated transition, the alignment of independent dynamical components, the collapse onto a constrained manifold, and the deterministic mapping into the discrete energy ladder together form a unified structural system. With the introduction of inlet-geometry modulation, this architecture acquires an additional degree of refinement: the resonance-alignment window becomes mode-dependent, and the deterministic state-selection outcome at the reversal boundary is conditioned on the manifold— $\mathcal{M}_{\text{nasal}}$ or $\mathcal{M}_{\text{oral}}$ —along which the system evolves.

The inlet geometry does not merely perturb the inflow profile; it functions as a structural control parameter. By altering the turbulence field, the pre-carinal velocity distribution, and the magnitude of the Venturi-induced gradient $G(t)$, the inlet pathway determines the curvature of the primary isotope-class trajectory $\mathbf{Ax}_I(t)$ and the timing and slope of its intersection with the Gaussian field envelope $B(t)$. The nasal pathway, with its higher resistance, smaller hydraulic diameter, and stronger shear-driven stratification, produces a steeper rise in $\mathbf{Ax}_I(t)$, a larger geometric amplification, and an earlier, more forceful resonance alignment. The oral pathway, with its broader inlet and weaker shear, yields a shallower rise, a reduced gradient, and a later, less sharply constrained alignment. This establishes a strict efficiency ordering:

$$\text{nasal} \succ \text{oral},$$

where \succ denotes greater structural efficiency in driving the system into the resonance-aligned activation window before the reversal boundary.

In this expanded view, the activation event is not an isolated phenomenon but the central organizing principle of the half-cycle. It binds the continuous geometry to the discrete state structure, enforces directional asymmetry, and reveals how selectable boundary conditions shape the system’s evolution. The inlet geometry determines not only the trajectory

curvature and amplification strength but also the manifold on which the system collapses and the discrete state into which it is forced at $t = 2.0$ s.

Taken together, these results demonstrate that resonance, geometry, modulation, and discrete selection coalesce into a single, structurally inevitable transition framework. The ventilation cycle is not merely a physiological oscillation but a mathematically organized system whose deterministic behavior emerges from the interplay of rising trajectories, geometric amplification, field modulation, and selectable inlet geometry. The model thus stands as a coherent synthesis of continuous-time dynamics and discrete state selection, revealing the invariant structural relationships that govern the system's behavior across the entire inflow interval.

Discussion. Figure 1.4 provides a direct visual demonstration of the structural consequences of inlet-geometry modulation. The nasal pathway, characterized by a reduced hydraulic diameter and increased resistance, generates a turbulence-conditioned velocity profile that steepens the ascending branch of $\mathbf{x}_I(t)$ and amplifies the Venturi-induced gradient $G(t)$. This convergence results in a higher peak amplitude, an accelerated intersection with the Gaussian envelope $B(t)$, and a more sharply defined resonance-alignment window. Conversely, the oral pathway yields a broader, lower-shear inflow profile that attenuates the curvature of $\mathbf{x}_I(t)$ and dampens the geometric amplification, thereby delaying the resonance alignment and reducing its derivative magnitude. These variances are not merely physiological contingencies but are the necessary structural consequences of the inlet geometry.

The figure thus substantiates Proposition 1.11.4: the nasal inlet geometry is structurally more efficient than the oral geometry in driving the system into the resonance-aligned activation window prior to the reversal boundary. The efficiency ordering nasal \succ oral is manifested in the comparative steepness, amplitude, and timing of the di-Oxy I peak, which governs the activation threshold. By integrating the turbulence field, the Venturi gradient, and the envelope intersection into a single visual framework, Figure 1.4 explicitly illustrates how selectable inlet geometry functions as a structural control parameter for deterministic state selection at $t = 2.0$ s.